A Delaminated Defect-Rich ZrO_2 Hierarchical Nanowire Photocathode for Efficient Photoelectrochemical Hydrogen Evolution

*Md Anisur Rahman, Joseph P. Thomas, and Kam Tong Leung**

An efficient way to combat the energy crisis and the greenhouse gas effect of fossil fuels is the production of hydrogen fuel from solar-driven water splitting reaction. Here, this study presents a p-type ZrO_2 nanoplate-decorated ZrO_2 nanowire photocathode with a high photoconversion efficiency that makes it potentially viable for commercial solar H_2 production. The composition of oxygen vacancy defects, low charge carrier transport property, and high specific surface area of these as-grown hierarchical nanowires are further improved by an hydrofluoric acid (HF) treatment, which causes partial delamination and produces a thin amorphous ZrO_2 layer on the surface of the as-grown nanostructured film. The presence of different types of oxygen vacancies (neutral, singly charged, and doubly charged defects) and their compositional correlation to the Zr^{x+} oxidation states ($4 > x > 2$) are found to affect the charge transfer process, the p-type conductivity, and the photocatalytic activity of the ZrO_2 nanostructured film. The resulting photocathode provides the highest overall photocurrent (–42.3 mA cm^{-2} at 0 V vs reversible hydrogen electrode (RHE)) among all the photocathodes reported to date, and an outstanding 3.1% half-cell solar-to-hydrogen conversion efficiency with a Faradaic efficiency of 97.8%. Even more remarkable is that the majority of the photocurrent (69%) is produced in the visible light region.

1. Introduction

With increasing global energy demand and climate change impact of CO_2 emission from fossil fuels, the production of chemical fuels from clean energy supplies has become one of the most urgent challenges for the modern world.[1–3] Photoelectrochemical splitting of water into hydrogen and oxygen by sunlight is an ideal renewable method of hydrogen production, and it represents an attractive, sustainable solution to the clean energy challenge.[4] Considerable efforts have been made in the past decade to achieve a solar-to-hydrogen conversion efficiency of more than 10% in order to become viable for practical applications.[5] Among the various efforts in improving a photoelectrochemical water splitting system, appropriate choice of photoelectrode materials (usually p-type or n-type semiconductors) that are compatible with solar energy conversion, particularly in the visible spectral region, is especially important. This is because material properties, such as optical absorption, energy band positions, and chemical stability, could greatly affect the system performance.[6–9] For commercially viable hydrogen production, the photoelectrochemical system must also be low-cost and be fabricated from abundant elements using a scalable manufacturing process.[10,11]

Due to their low cost and ready availability, many metal oxides, such as Fe_2O_3,[6] TiO_2,[7] ZrO_2,[8] and Cu_2O,[9] have attracted a lot of attention as candidate photoelectrode materials for photoelectrochemical conversion of solar energy into chemical fuels. However, their large bandgaps (≈3 eV) and relatively fast electron–hole recombination rates limit their photoconversion efficiency to less than 0.1% in the visible region of the solar spectrum.[12,13] To overcome these drawbacks, several strategies have been attempted, and they include doping with impurity elements,[14,15] use of metal-semiconductor[16–18] and semiconductor–semiconductor heterojunctions,[19,20] thermal annealing in a reductive environment,[21] surface passivation,[9] and incorporation of amorphous metal oxides (because of their abundant surface defects and lattice dislocations that are crucial for providing appropriate defect states in the bandgap and a large number of reaction sites).[22] Although these strategies are capable of improving light absorption in metal oxides, the resulting overall water splitting efficiencies fall well below the respective theoretical maximum efficiencies of 10–20%.[9,23] This discrepancy could be due to low specific surface area, generation of only surface defects instead of bulk defects in reductive environments, and presence of large numbers of recombination centers in doped, amorphous, and heterojunction semiconductors.[9,15,20,24,25] Moreover, the photoelectrochemical activity of thin-film electrode is generally restricted to the top surface, as the underside (i.e., the bottom) surface of the base film is in direct contact with the conductive substrate and out of reach of the electrolyte, making it unusable for photoelectrochemical reactions. By partially delaminating the thin film, it is possible to expose the bottom surface of the base film, thereby potentially doubling the active area, for the photoelectrochemical

Dr. Md A. Rahman, Dr. J. P. Thomas, Prof. K. T. Leung
WATLab and Department of Chemistry
University of Waterloo
200 University Avenue West, Waterloo, ON N2L3G1, Canada
E-mail: tong@uwaterloo.ca

DOI: 10.1002/aenm.201701234

reactions. To improve the charge-carrier collection, it is also extremely important to develop a photocatalyst material with not only high crystallinity and large surface area, but also a large amount of oxygen vacancies, short charge-transfer length, and special morphology for enhancing performance in photoelectrochemical water splitting.

Zirconium dioxide (ZrO_2) is one of the most promising water reduction materials because of its abundance (over even copper) in the earth's crust, low cost, strong photoreducing power, high photostability in acidic and alkaline media, nontoxicity, and compatible band-edge positions with the hydrogen evolution potential.[26,27] To date, the use of ZrO_2 in photodecomposition of water has been limited due to its wide bandgap and limited absorptivity of visible light. Clearly, there is an acute need to develop ZrO_2 catalysts with a reduced bandgap. Compared to thin films, the 1D nanostructures, such as hierarchical nanowires and nanotubes, with their improved charge transfer dynamics and large specific surface area offer abundant surface active sites that could potentially enhance the photoelectrochemical activity.[28] However, the synthesis of oxygen-deficient 1D single-crystalline ZrO_2 nanowires (with reduced bandgaps) by catalyst-assisted vapor–liquid–solid (VLS) growth,[29] as one of the most popular approaches to synthesize single-crystalline nanostructures, has thus far been unsuccessful due to the difficulties caused by the low vapor pressures and high melting points of Zr (1789 °C) and ZrO_2 (2715 °C).[30] Moreover, in order to fabricate 1D nanostructures by the VLS growth approach above 1079 °C (the eutectic point of Au-Zr),[31] a dielectric buffer layer for the Si substrate is required to prevent the formation of silicides with the sensitive catalysts (such as Au).[32] Such a dielectric buffer layer could, however, impede direct flow of photogenerated carriers from the nanostructured film to the conductive substrate. Here, we use a one-step catalyst-assisted pulsed laser deposition technique to grow highly oxygen-deficient, p-type hierarchical ZrO_2 nanowires with the aid of gold nanoisland (GNI) catalysts on an Si substrate with an SiO_2 buffer layer of appropriately optimized thickness. We show that the as-grown ZrO_2 hierarchical nanowires are highly oxygen-deficient and the use of an HF treatment creates a thin amorphous ZrO_2 layer on the surface of crystalline ZrO_2 that significantly improves carrier transport and provides electrochemically active sites not found on planar structures. The partial dissolution of the interfacial SiO_2 layer in HF also enables us to produce a flaky nanostructured film with considerably larger surface area by partially exposing the underside surface of the nanostructured film. We demonstrate the ultrahigh photocatalytic performance of these flaky, defect-rich hierarchical nanowire films in a photoelectrochemical water splitting reaction for the first time. Even more extraordinary are that they have the highest overall photocurrent (−42.3 mA cm^{-2} at 0 V vs RHE) among all the photocathodes reported to date and their photoactivity is predominantly driven by visible light (>400 nm). This simple post-treatment technique can also be used to improve the performance of hierarchical nanostructured films of other transparent oxides such as TiO_2 and Ta_2O_5. We believe that the broad appeal of the present approach will open up an entirely new parameter space for design and optimization of nanostructured thin films for enhanced photoelectrochemical performance.

2. Results and Discussion

2.1. Synthesis and Characterization of ZrO_2 Nanostructures

GNIs have been fabricated on the Ox-Si substrate by magnetron sputtering a thin layer of Au for 10 s followed by annealing at 600 °C in air for 1 h. The resulting GNIs exhibit a near-Gaussian size distribution, with a mean diameter of 50 ± 10 nm (**Figure 1**a). Evidently, the corresponding ZrO_2 nanowires, grown on the GNI/Ox-Si template at 770 °C, are found to be randomly oriented with respect to the substrate plane and the nanowires appear tapered (Figure 1b). Closer examination reveals that individual nanowire corresponds to a string of nanoplates stacked horizontally on top of one another with a gap spacing of ≈3 nm (Figure 1b, inset). The nanoplate appears to have a cross section with a distorted polygon shape and a thickness of ≈6 nm. The scanning electron microscopy (SEM) images in Figure 1c1–1c4 show that the angle, size, and distribution of the stacking nanoplates along the main trunks of the nanowires could change from nanowire to nanowire (Figure 1c1). In some nanowires, the nanoplates are stacked almost perpendicularly (≈90°) along the core nanowire length (Figure 1c2), while the angles of the other nanoplates range from 45° to 70° (Figure 1c3). A mixture of two orientations is also observed in some of the nanowires (Figure 1c4). Smaller nanoplates with side lengths of 10–20 nm are observed at the tip, while those at the base are found to be larger with side lengths of 50–70 nm, and the tip of the nanowire trunk is covered by more nanoplates than the base. The corresponding transmission electron microscopy (TEM) image confirms the single-crystalline nature of the stacking nanoplates, with an interplanar spacing (5.1 Å) consistent with the (100) plane of monoclinic ZrO_2 (Figure 1d). Close inspection reveals that the nanoplates have their roots inside the core nanowire trunk surface and they appear firmly attached to the nanowire trunk.

In a separate experiment, pulsed laser deposition (PLD) growth of ZrO_2 on an Ox-Si substrate without any GNI catalyst produces nanobricks with an interplanar spacings of 2.9 and 2.5 Å, corresponding to the (101) and (110) planes of tetragonal ZrO_2, respectively (Figure 1e). Closer examination of the hierarchical nanowire film shown in Figure 1b reveals the presence of similar nanobricks among the bases of the hierarchical nanowires. This suggests concurrent vapor–solid growth of nanobricks in regions where there is no catalyst in the nanowire sample. However, PLD growth at 770 °C on a GNI/Ox-Si template with the SiO_2 layer thickness below ≈10 nm produces mainly nanopopcorn-like film (Figure S1, Supporting Information), which is due to the formation of Au-silicide by interfacial reaction between the GNI and Si.[33] The thicker SiO_2 layer (10 nm) on the Ox-Si template (Figure 1a) prevents Au diffusion into the substrate and the subsequent Au-silicide formation. A SiO_2 layer with the appropriate thickness (of ≈10 nm) is therefore extremely important for enabling VLS growth in the present PLD method.

The size of the nanoplates and consequently the morphology of the hierarchical nanostructures can be tuned by varying the size of the GNI catalysts. The average size of the GNIs is controlled by the thickness of the gold layer and the annealing temperature. Evidently, PLD growth of ZrO_2 at 770 °C on a GNI/Ox-Si template with smaller GNIs (15 ± 5 nm) (**Figure 2**a1) produces single-crystalline regular nanowires, i.e., without any

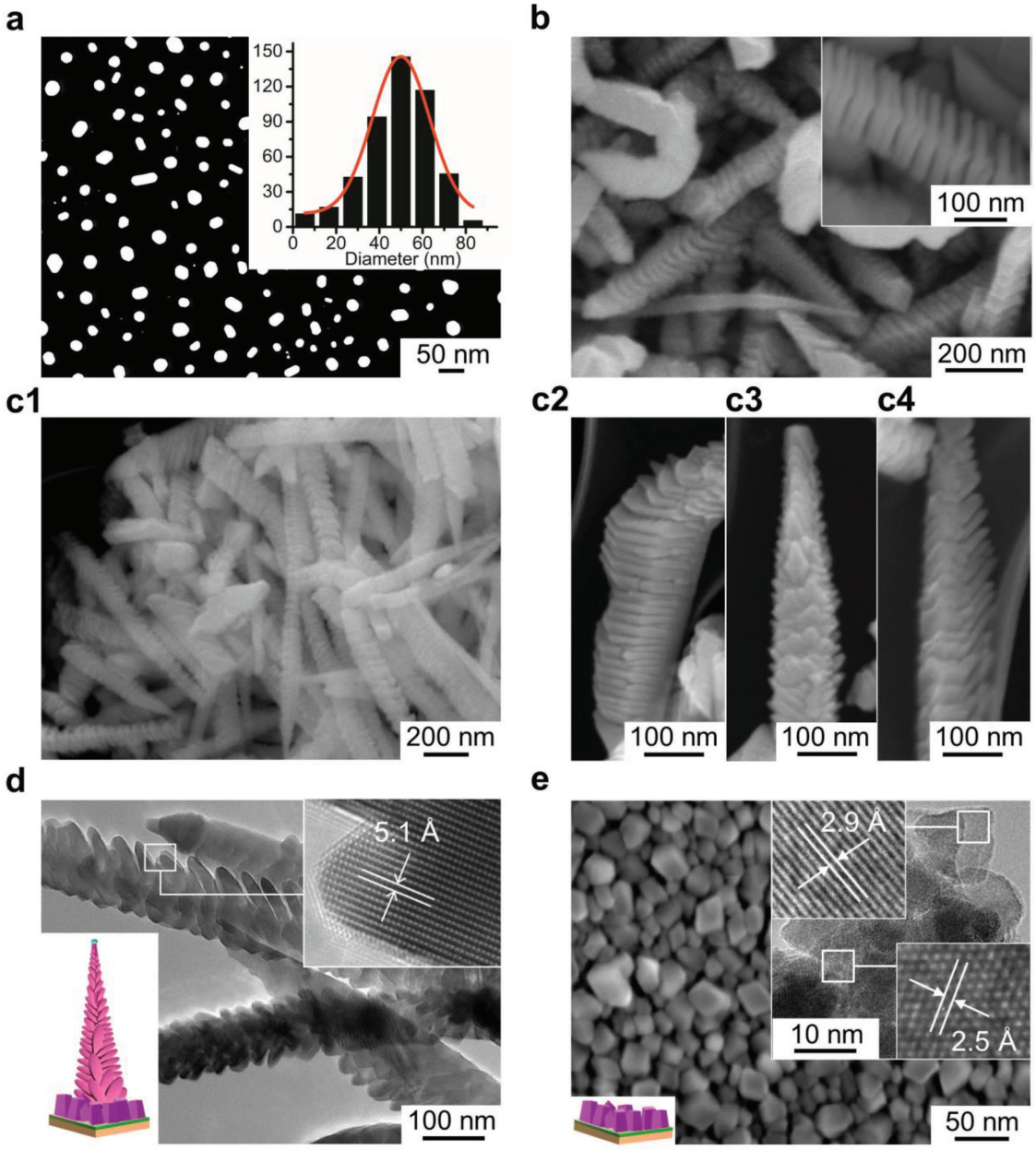

Figure 1. a) SEM image of typical gold nanoislands (GNIs), with its corresponding size distribution (inset), formed on the Ox-Si substrate by magnetron sputtering a thin layer of Au for 10 s followed by annealing at 600 °C in air for 1 h. b) SEM images of PLD-grown ZrO_2 hierarchical nanowires on the GNI/Ox-Si template at 770 °C in 200 mTorr of Ar for 90 min, and c1–c4) ZrO_2 hierarchical nanowires scrapped off from the GNI/Ox-Si template, taken after dispersing onto holey carbon TEM copper grids. d) TEM images of a typical ZrO_2 hierarchical nanowire. e) SEM image of ZrO_2 nanobricks PLD-grown on bare Ox-Si substrate (without any GNI) in 200 mTorr of Ar at 770 °C for 90 min. In (d) and (e), the lower-left insets show schematic representations of the respective PLD-grown nanostructures, while the upper-right insets show high-resolution TEM images of selected areas of the respective nanostructures.

nanoplates (Figure 2a2), with an interplanar spacing of 2.6 Å corresponding to the (002) plane of bulk monoclinic ZrO_2 (Figure S2, Supporting Information). On the other hand, PLD growth on a GNI/Ox-Si template with 30 ± 10 nm GNIs (Figure 2b1) produces hierarchical nanowires with small nanoplates and a gap spacing of 2–3 nm (Figure 2b2). For GNI/Ox-Si template with further increase in the average gold catalyst size to 90 ± 20 nm (Figure 2c1), octopus-like nanowire assemblies are formed (Figure 2c2), of which more than one hierarchical nanowires are grown from a single large Au nanoparticle (Figure 2c2, inset), and the size of the nanoplates varies from wire to wire (not shown). These results therefore illustrate the importance of delicate control of the catalyst size in effecting the desired morphologies of the as-grown ZrO_2 nanostructures. A critical GNI size of 30–60 nm is necessary for the successful formation of the hierarchical nanowires while any GNI size less than 20 nm or greater than 70 nm would be ineffective in producing the hierarchical nanowires.

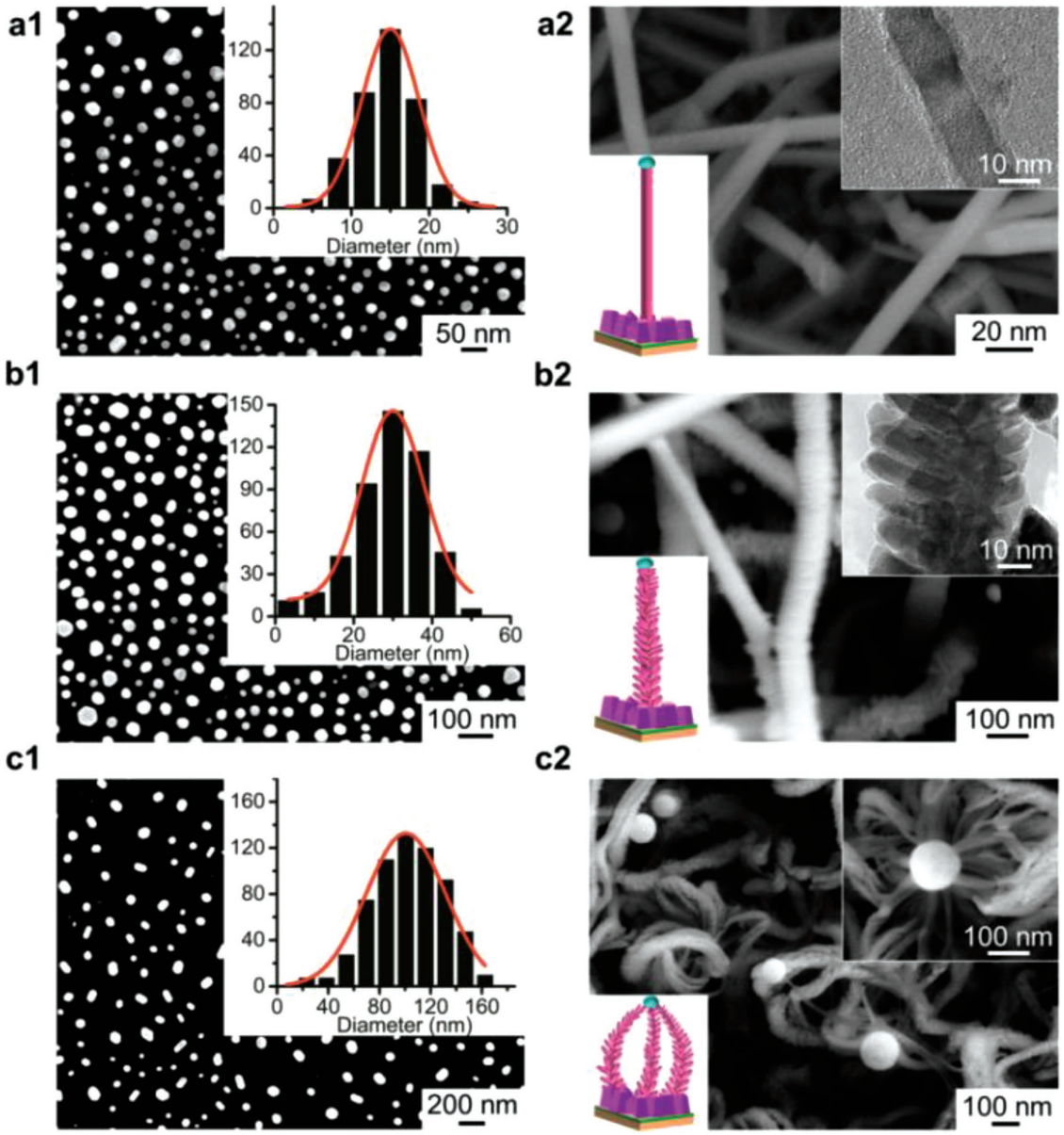

Figure 2. a1,b1,c1) SEM images of typical gold nanoislands (GNIs), with the corresponding near-Gaussian size distributions (insets), formed on Ox-Si templates by magnetron sputtering a gold target for a1) 3 s, b1) 6 s, and c1) 15 s followed by annealing in air at 600 °C for 1 h. SEM images of a2) regular nanowires, b2) hierarchical nanowires with small nanoplates, and c2) octopus-like hierarchical nanowires PLD-grown in 200 mTorr Ar at 770 °C for 90 min on the respective GNI/Ox-Si templates shown in (a1), (b1), and (c1). The corresponding lower-left insets show schematic models of the as-grown nanostructures, while the upper-right insets in (a2, b2) and in (c2), respectively, depict the magnified TEM images and SEM image of the respective as-grown nanostructures.

Our proposed growth mechanism for the hierarchical ZrO_2 nanowires is shown schematically in **Figure 3**. The initial gold nanoisland formation on the Ox-Si substrate provides the essential catalysts for VLS growth. At the start of the VLS growth, a ZrO_2 nanowire trunk pushes up and detaches a GNI from the Ox-Si substrate. As the VLS growth continues, a fraction of the Au atoms are evaporated from the bulk Au catalyst at the tip of the nanowire trunk, and they then get readsorbed on the surface of nanowire trunk. These readsorbed Au atoms become additional nucleation sites, enhance the absorption rate of incoming ZrO_2 vapors, and promote ZrO_2 nanoplate formation. The longer exposure of the base to the incoming ZrO_2 vapor compared to the tip results in larger nanoplates at the base and smaller nanoplates at the tip of the nanowire trunk, thus accounting for the observed tapered shape of the hierarchical nanowire structure.

Figure S3 (Supporting Information) shows the corresponding glancing-incidence X-ray diffraction (XRD) patterns of the as-grown hierarchical nanowires (Figure 1b) and nanobricks (Figure 1e). The prominent diffraction peaks of the hierarchical nanowire and nanobrick films are found to be in excellent accord with the monoclinic (PDF2 #01-083-0940) and

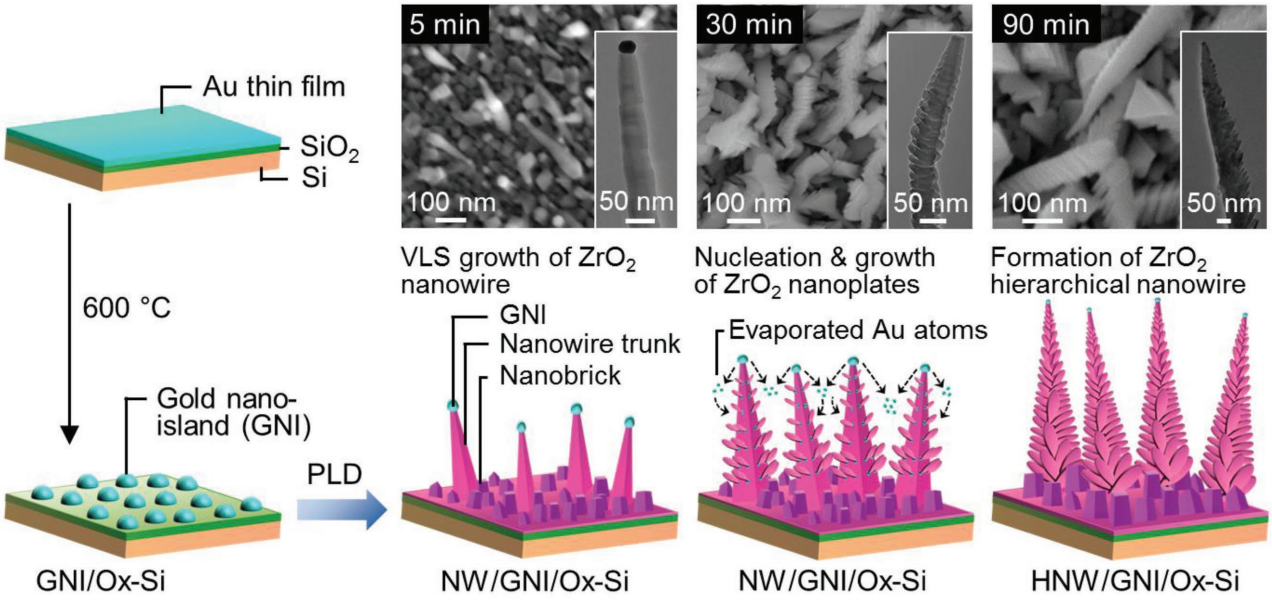

Figure 3. Schematic diagram of the proposed catalyst-assisted vapor–liquid–solid (VLS) growth mechanism for typical ZrO_2 hierarchical nanowires.

tetragonal ZrO_2 reference patterns (PDF2 #01-080-0784), respectively. The additional minor contributions from the tetragonal ZrO_2 phase and face-centered cubic (FCC) phase of metallic Au (PDF2 #03-065-8601) in the hierarchical nanowire films can be attributed to the presence of the nanobricks between the nanowires and that of the GNI catalysts, respectively. As with the hierarchical nanowires (Figure 1b), the regular nanowires without nanoplates (Figure 2a2), the hierarchical nanowires with small nanoplates (Figure 2b2), and octopus-like hierarchical nanowires (Figure 2c2) also exhibit similar XRD patterns with predominant monoclinic ZrO_2 features (not shown). The XRD and TEM results therefore both support that the PLD-grown ZrO_2 regular nanowires and hierarchical nanowires are predominantly monoclinic, while the nanobricks among these nanostructures (similar to those that make up the nanobrick film) are predominantly tetragonal ZrO_2. Moreover, the single-crystalline nature of the regular nanowires (Figure S2, Supporting Information) suggests that the main trunks of individual hierarchical nanowires are also single-crystalline, monoclinic ZrO_2.

The presence of secondary structures such as the nanoplates around the trunk of the nanowire has dramatically increased the surface area of the hierarchical nanowire relative to the regular nanowire. These secondary nanoplates are therefore expected to greatly increase the amount of catalytically active sites (per illumination photocathode area) and consequently photoelectrochemical water splitting activity. However, among the base of the hierarchical nanowires are the nanobricks, and the entire ZrO_2 nanostructured film is attached to the Si substrate through a 10 nm thick interfacial SiO_2 layer (**Figure 4**a,c). The presence of a relatively thick dielectric layer between the ZrO_2 nanostructured film and the Si substrate is expected to impede direct transfer of photogenerated charge carriers from the nanostructured film to the substrate. To get collected by the external contact (placed at the edge and on the top of the film), the charge carriers photogenerated in the film must travel across the base layer to the external contact point (Figure 4a). Consequently, a majority of the charge carriers might be lost due to recombination at the defect sites in the base layer. As with the majority of the thin-film-based photoelectrodes, the electrolyte is exposed to and therefore photoelectrochemical activity is restricted to the top side of the film (Figure 4c). In contrast, as the underside surface of a partially delaminated thin film is partially detached from the substrate or supporting layer (Figure 4b), the film might have a direct contact with the Si substrate, and the electrolyte is in contact with and could therefore access both the top side and underside surfaces of the film. The resulting photoactivity is expected to increase considerably depending on the extent of the delamination. This partial delamination architecture could also improve light absorption, because a more textured film could scatter the light more efficiently than a planar film. More importantly, for the substrate-sensitive nanostructured growth (as in the present case), partial delamination could remove part of the dielectric layer such that transport of the photogenerated carriers could proceed directly between those parts of the delaminated nanostructured film that are in better contact with the conductive substrate and the external contact (Figure 4b). The photoelectrochemical properties could be further enhanced by creating a thin amorphous ZrO_2 layer onto the surface of single-crystalline ZrO_2. With both structural disorder-related defects (free volume) and nonstoichiometric (oxygen vacancy) defects, the amorphous phase usually possesses more defect states[25] and offer a larger number of electrocatalytic active sites[34] than the crystalline phase of the same composition. The carriers photogenerated in a thin amorphous layer could also be easily collected by their single-crystalline core, which significantly affects the corresponding electrical conducting properties. Partial delamination and the formation of a thin amorphous layer on the surface of crystalline nanostructures therefore offer significant performance benefits in the development of advanced metal-oxide catalysts.

To date, there is no report on direct method of producing partially delaminated nanostructured thin films. Perhaps an

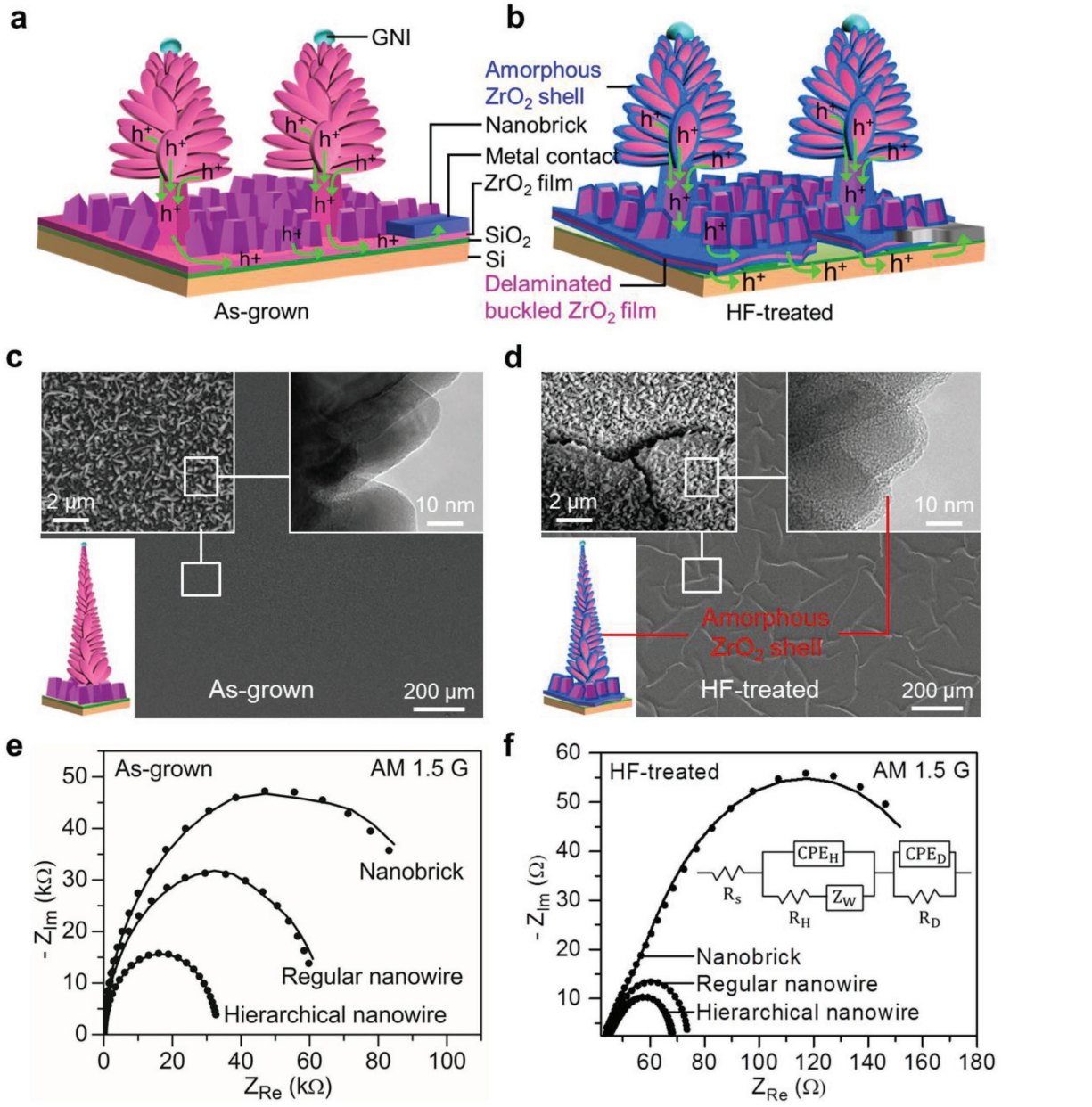

Figure 4. Schematic models of the hierarchical nanowire film a) before and b) after the HF treatment. SEM images of c) as-grown and d) HF-treated ZrO_2 hierarchical nanowire films, with magnified views of selected areas in insets. The corresponding lower-left insets in (c) and (d) show schematic models of ZrO_2 nanostructures before and after HF treatment, respectively, while the upper-left and upper-right insets depict the magnified SEM and TEM images of the respective nanostructures. Nyquist plots of e) as-grown and f) HF-treated hierarchical nanowire samples under illumination of simulated sunlight (100 mW cm^{-2}). The experimental data (solid circles) are collected in a frequency range between 0.01 and 100 Hz with an AC voltage amplitude of 10 mV and a DC bias of 0.2 V (vs RHE), and they are fitted with (f, inset) an equivalent circuit model (solid lines). In the equivalent circuit model, the series resistance (R_S), the resistance (R_D), and chemical capacitance or constant phase element (CPE_D) of the semiconductor depletion layer in an R_C circuit, along with the charge-transfer resistance in the Helmholtz layer (R_H), the Warburg diffusion impedance (Z_W), and the capacitance of the electrochemical double layer (CPE_H) in a second RC circuit are connected in series.

even bigger challenge is the creation of a uniform, thin amorphous layer on the surface of a crystalline oxide film. Here, we develop a facile post-treatment to create such a nanoarchitecture to massively increase the photoactivity and the charge transport for photoelectrochemical reactions, by simply soaking the as-grown ZrO_2 hierarchical nanowire film in a 0.01 M HF solution for 1 h. Evidently, the HF treatment produces a thin amorphous layer on the surface of crystalline oxide (Figure 4d, right inset), and "cracking" is found to develop across the film, likely along fault lines with poor adhesion between the film and the substrate. This HF treatment converts the smooth film (Figure 4c) into a "flaky" film with a random-stone-like pattern (Figure 4d). Partial dissolution of the underlying SiO_2 layer also causes residual compressive stress near the edge of the flakes

as a result of the mismatched strains between the detached and attached portions of the film. This mismatched strain occurs upon cooling from high-temperature deposition and arises as a result of the differences in the thermal expansion coefficients of the film and the supporting SiO_2 layer (and the substrate). As the supporting layer (and the substrate) is much more massive than the film itself, it contracts more freely and consequently imposes a strain on the film in all directions parallel to the interface. As a result, extension of channel cracks and buckling in the film occur (at the edges of the flakes) in the absence of the SiO_2 layer. More importantly, TEM analysis of the base of hierarchical nanowire film (Figure S4, Supporting Information) shows that there is also an amorphous layer on the underside surface of the buckled film, which could provide direct contact between the film and the Si substrate and improve the charge carrier collection. Similar results are also obtained for the nanobrick and nanowire films (not shown). Both X-ray diffraction and TEM analyses also confirm that the HF treatment does not affect the crystallinity of the films with the formation of the amorphous layer occurring only on the perimeters of the films.

To identify the chemical nature of the ZrO_2 hierarchical nanowire film before and after the HF treatment, we compare, in **Figure 5**, the X-ray photoelectron spectroscopy (XPS) spectra of Zr 3d and O 1s regions of the nanobrick, regular nanowire, and hierarchical nanowire films. The prominent Zr $3d_{5/2}$ peak at 182.4 eV corresponds to the Zr^{4+} state for ZrO_2, while the residual intensity between the Zr^{4+} feature (at 182.4 eV) and metallic Zr^0 feature (at 178.3 eV) could be fitted with two components: ZrO_{x1} ($2 > x1 > 1.5$) and ZrO_{x2} ($1.5 \geq x2 > 1$). The prominent O 1s peak located at 530.3 eV is attributed to O^{2-} in ZrO_2 and the O 1s feature located at 532.64 eV attributed to the SiO_x ($2 > x > 1.5$) species. The residual O 1s peaks between the ZrO_2 and SiO_x features can be assigned to oxygen anions in the oxygen-deficient ZrO_{x1} and ZrO_{x2} species within the matrix. The apparent relative increase of SiO_x species in the HF-treated sample is due to cracks and openings in the partially delaminated film, which allow more exposure of the underlying Si substrate compared to the as-grown nanowires.

Due to a fairly attractive Madelung potential of excess electrons in oxygen-deficient ZrO_2,[35] the oxygen vacancy defects of ZrO_2 can have three different charge states: neutral, singly charged, and doubly charged defects. The formation of a neutral oxygen vacancy would result in two electrons to remain at the oxygen vacancy site, and there is therefore no apparent effect on the neighboring Zr^{4+} oxidation states. For the singly charged oxygen vacancy, one electron would remain at the singly charged oxygen vacancy site, with the other electron in the corresponding Zr atom leading to a Zr^{3+} ($4d^1$) ion. For the doubly charged oxygen vacancy, two electrons from the vacancy site could be located at two nearest-neighbor Zr sites [leading to two Zr^{3+} ($4d^1$) ions] or both at one Zr site [leading to a Zr^{2+} ($4d^2$) ion]. Different lattice relaxations associated with the differently charged oxygen vacancies change the corresponding O 1s and Zr 3d binding energies in oxygen-deficient ZrO_2.

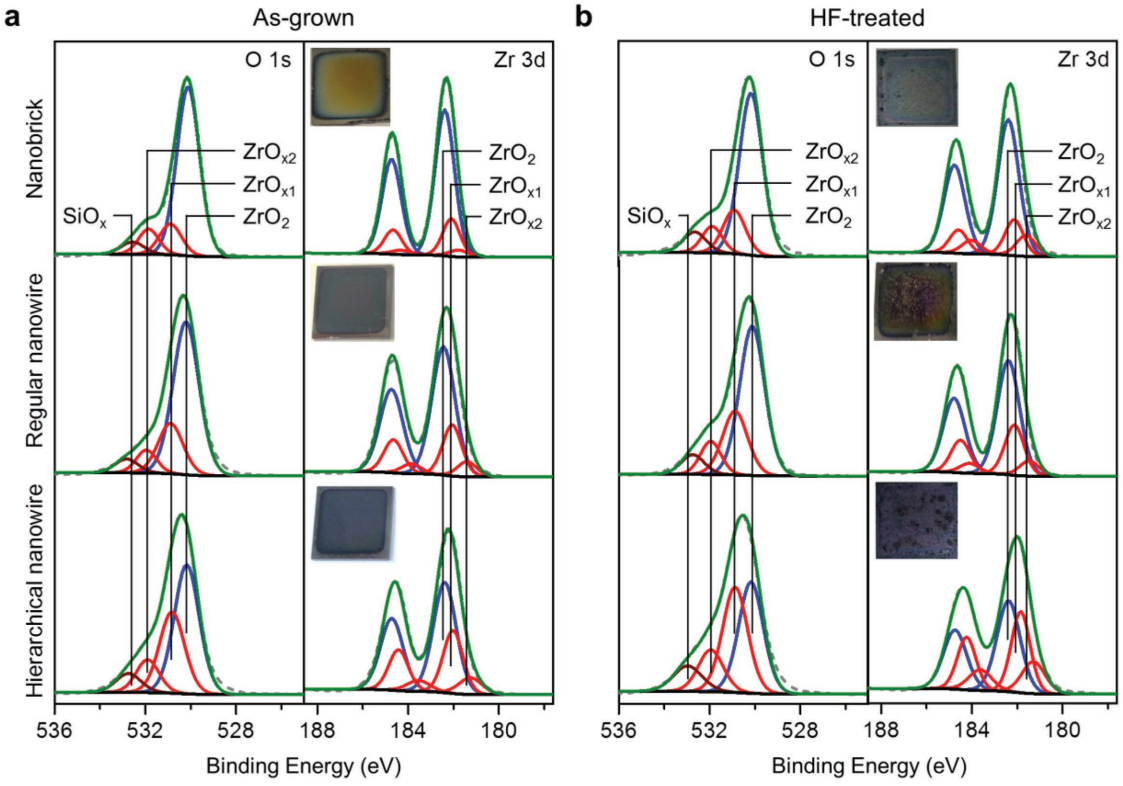

Figure 5. XPS spectra of Zr 3d and O 1s regions of a) as-deposited, and b) HF-treated ZrO_2 nanobrick (top row), regular nanowire (middle row) and hierarchical nanowire films (bottom row). In addition to the ZrO_2 and SiO_x ($2 > x > 1.5$) features, two sets of oxygen vacancy defect features corresponding to ZrO_{x1} ($2 > x1 > 1.5$) and ZrO_{x2} ($1.5 \geq x2 > 1$) are used to fit the residual intensities. Photographs of the as-grown and HF-treated nanostructured samples are shown as insets in (a) and (b), respectively.

Density functional theory calculations have also confirmed that the singly and doubly charged oxygen vacancies have larger lattice relaxation effects than the neutral oxygen vacancies.[35] The decrease in electron charge density for the $O-Zr^{3+}$ bond (relative to the $O-Zr^{4+}$ bond) results in less screening of the O 1s electrons, which consequently increases the effective nuclear charge and leads to an increase in the O 1s binding energy and a corresponding decrease in the Zr 3d binding energy. The O 1s and the corresponding Zr 3d peaks for ZrO_{x1} and ZrO_{x2} therefore correspond to the singly charged and doubly charged oxygen vacancies, respectively, while those for the neutral oxygen vacancy defect reside with the respective features for ZrO_2. Along with the discernible intensity variations found for the O 1s and Zr 3d states for the ZrO_{x1} and ZrO_{x2} components, the minor differences in the binding energy positions and in the full widths at half maximum reflect the differences in the relative compositions of these different types of oxygen vacancies in a particular sample. The O 1s and the Zr 3d intensity percentages for the ZrO_{x1} and ZrO_{x2} components of the respective total intensities (i.e., ZrO_2+ZrO_{x1}+ZrO_{x2}) for the as-grown and the HF-treated nanostructures are summarized in Table S1 (Supporting Information). The total defect intensity is found to increase after the HF treatment for all three nanostructured samples. This can be attributed to the formation of the thin amorphous ZrO_2 layer and to flaking and buckling of the film (as a result of residual compressive stress caused by removal of the SiO_x layer), all of which generate a larger amount of defects in the partial delamination process. For the as-grown and HF-treated samples, the summed defect intensity (ZrO_{x1}+ZrO_{x2}) appears to follow the descending trend: hierarchical nanowire > regular nanowire > nanobrick, which is consistent with a similar trend in the specific surface area.

The increases in the defect density and in the surface roughness due to buckling and formation of an amorphous layer also change the colors of the HF-treated samples. For the as-grown nanostructured samples, the color changes from light blue (nanobrick) to bluish black (regular nanowire), and to grayish black (hierarchical nanowire), due to the increasing amount of oxygen vacancy defects within the nanostructures (Figure 5a, insets). Similarly, in the partially delaminated samples, the color also changes due to differences in the compositions of the oxygen vacancies and in the surface roughness of the films. The contrast differences between the HF-treated samples and the respective as-deposited samples further confirm the buckling-driven delamination process. The corresponding reflectance spectra follow essentially the same profile over the 320–680 nm range, with the magnitude following the descending trend: nanobrick > regular nanowire > hierarchical nanowire, and the absorbance following the opposite trend (Figure S5, Supporting Information). However, the HF-treated samples exhibit ≈10% lower reflectance than the respective as-deposited samples, which could be due to a higher number of defect states within the amorphous ZrO_2 layer,[25] and more scattering caused by buckling of the delaminated films. The absorbance of the ZrO_2 nanostructures in the visible region could therefore be attributed to the existence of defect states within the bandgap, the overlap and hybridization of which could lead to impurity bands within the bandgap.[36] Moreover, both the as-grown and HF-treated ZrO_2 samples retain their individual color profiles upon storage in an ambient atmosphere for over a year, which indicates that the defects are located in the bulk and not just at the surface of these nanostructures.

The minor deviation from perfect stoichiometry and the improved electrical contact between the film and the Si substrate (due to partial dissolution of interfacial SiO_2 layer and formation of amorphous ZrO_2 layer on the underside surface of the buckled film, as illustrated in Figure 4b,d) are expected to produce significant enhancements in the electrical and optical properties of these partially delaminated ZrO_2 nanostructured films. Figure 4e,f shows the corresponding Nyquist plots for the nanostructured films before and after the HF treatment under simulated sunlight illumination obtained by potentiostatic electrochemical impedance spectroscopy. The electrical parameters obtained by fitting the experimental data with the model equivalent circuit (Figure 4f, inset) are summarized in Table S2 (Supporting Information). The fitted data show that the charge transfer resistances R_D have decreased by three orders of magnitude, while R_H have also decreased but to a lesser extent after the HF treatment. For both as-grown and HF-treated nanostructured films, the charge-transfer resistances decrease in the following order: nanobrick > regular nanowire > hierarchical nanowire, in close correlation with the opposite trends in the specific surface area, observed amounts of oxygen vacancy defects, and optical absorbance. The substantial reduction in the charge-transfer resistance at the depletion layer (R_D) between regular nanowires and hierarchical nanowires indicates that the nanoplates of the hierarchical nanowires contain a larger amount of oxygen vacancy defect states. Interestingly, the reduction in R_D of the HF-treated hierarchical nanowires with respect to that of the HF-treated regular nanowires is considerably smaller than the reduction between these nanowires before the HF treatment, which suggests that the partial removal of SiO_x and formation of the amorphous ZrO_2 layer in the partial delamination process have a much greater effect in lowering the charge-transfer resistance.

Several defect bands may occur as a result of the overlap and hybridization of the defect states, which in effect lead to a reduction in the observed optical bandgap. These defect states and their imprint on the electronic band structure may also change the carrier type (p- or n-type) of the resulting sample. In the present study, all the nanostructured samples are found to have p-type conductivity with a Hall effect coefficient of $\approx 4.6 \times 10^{-4}$ cm^3 C^{-1}. The observed p-type conductivity suggests that the presence of singly charged and doubly charged oxygen vacancies creates an acceptor band above the valance band maximum, similar to that found for acceptor-impurities in metal oxides.[37] The improved visible light absorbance, lower charge-transfer resistance, and a larger amount of defects in the partially delaminated, hierarchical nanowire sample promise an exceptional photocatalyst for visible sunlight-driven reactions and applications.

2.2. Photoelectrochemical Properties

In order to evaluate the photocatalytic activity of the aforementioned nanostructures for photoelectrochemical water splitting reaction, we employ the as-grown and HF-treated ZrO_2

nanobrick, regular nanowire, and hierarchical nanowire films as the photocathodes. The photocurrent spectra have been obtained for an illuminated sample area of 0.5 cm^2 under simulated sunlight illumination at 100 mW cm^{-2} (i.e., 1 sun) from a 300 W Xenon lamp coupled with an AM 1.5G filter. For the as-grown nanostructured films, the photocurrent density measured at 0 V versus RHE for the hierarchical nanowire film (−12.9 mA cm^{-2}) is found to be 3.6, and 2.0 times those of the nanobrick (−3.6 mA cm^{-2}) and regular nanowire films (−6.4 mA cm^{-2}), respectively (**Figure 6**a). It should be noted that the photocurrent density reported in the present work corresponds to the difference between light-on and dark current densities at 0 V versus RHE. On the other hand, the photocurrent density of the partially delaminated hierarchical nanowire film, obtained after the HF treatment, is found to increase stupendously to −42.5 mA cm^{-2}, i.e., ≈3.3 times that of the as-grown hierarchical nanowire film (−12.9 mA cm^{-2}, Figure 6b). For the delaminated regular nanowire and nanobrick films, the respective photocurrent densities have also increased to −18.7 mA cm^{-2} (by 2.9 times from −6.4 mA cm^{-2}) and to −9.2 mA cm^{-2} (by 2.6 times from −3.6 mA cm^{-2} of the respective as-grown nanostructured films). We have also characterized and obtained essentially negligible photocatalytic activity for the pristine Ox-Si substrate (Figure 6a, inset), and for the Si substrate after the as-grown hierarchical nanowire film has been completely removed (Figure S6, Supporting Information; and Figure 6b, inset) under the same conditions (designated here as delaminated Si sample). The photogenerated holes in Si cannot be easily transferred to the valence band of the ZrO_2 nanostructured film, likely due to a significant barrier at the junction resulting in carrier recombination in Si.[38] The significantly higher photocurrent density observed for the HF-treated hierarchical nanowires (and HF-treated regular nanowires) can therefore be attributed only to the photogenerated charge carriers from the ZrO_2 nanowires themselves and not the substrate.

Since stoichiometric ZrO_2 has wide bandgaps: monoclinic (3.58 eV), tetragonal (4.07 eV), and cubic (3.26 eV),[39] its photoelectrochemical activity is expected to come mainly from UV light illumination. This creates an inherent disadvantage for ZrO_2 (and other transparent conductive oxide materials with similar wide bandgaps) for solar-light driven applications, because UV light (<400 nm) represents only 5–8% of the overall AM 1.5G light. In order to determine the photoresponse arising from separate UV and visible spectral illuminations, we couple the AM 1.5G light with appropriate short-pass (<400 nm) and long-pass filters (>400 nm). As shown in Figure 6c, the

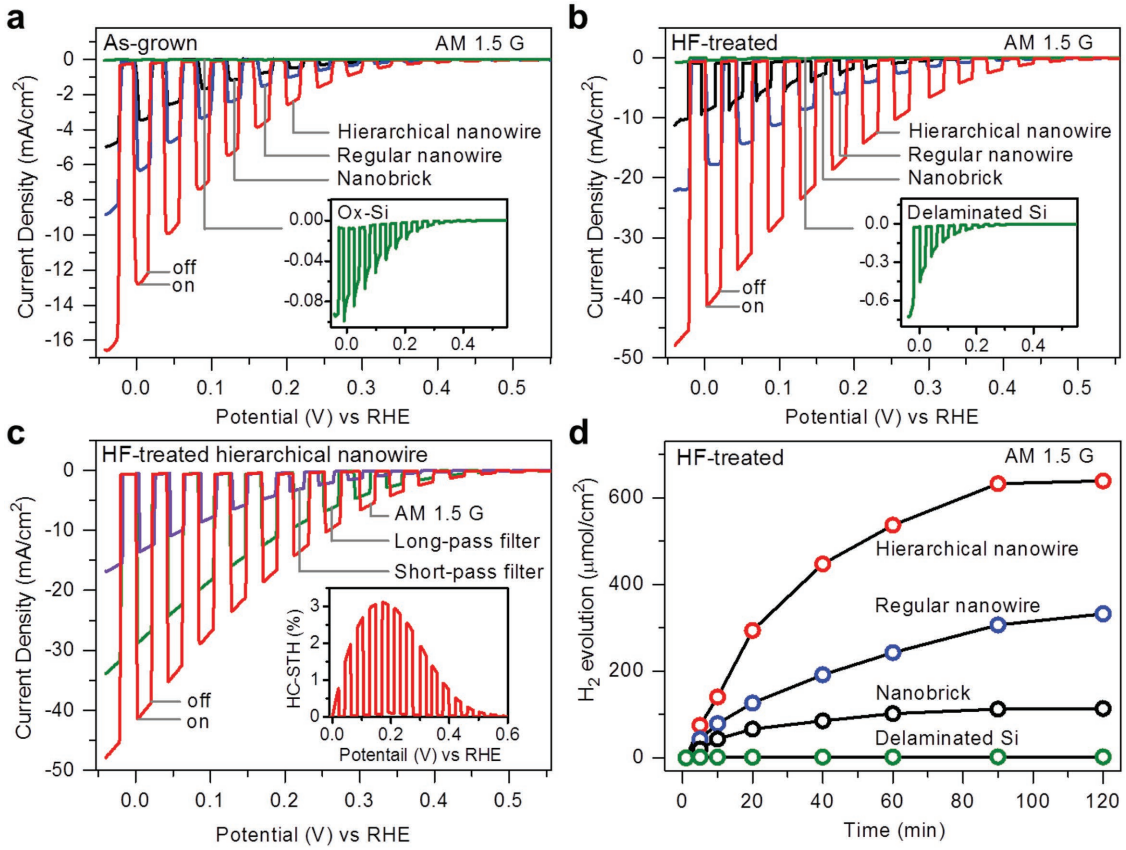

Figure 6. Current density measured by linear sweep voltammetry as a function of applied potential for a) as-grown and b) HF-treated ZrO_2 nanostructured film photocathodes, and for HF-treated hierarchical nanowire film photocathodes obtained with c) short-pass and long-pass filters. The insets in (a) and (b) show the linear sweep voltammograms of Ox-Si and Si substrate after complete delamination of hierarchical nanowire film, respectively, while the inset in (c) shows the half-cell solar-to-hydrogen (HC-STH) conversion efficiency of HF-treated hierarchical nanowire film. d) Time profiles of H_2 evolution of HF-treated ZrO_2 nanostructured films and of the delaminated Si substrate (i.e., after complete delamination of hierarchical nanowire film) at the applied voltage that gives the maximum HC-STH conversion efficiency [0.2 V (vs RHE)] for 2 h.

photocurrent density of the partially delaminated hierarchical nanowire film is reduced from –42.5 to –29.3 mA cm^{-2}, i.e., by only 31%, when the long-pass filter is coupled with the AM 1.5G filter, and to a significantly lower current density (–14.2 mA cm^{-2}, i.e., by more than 66%) when the short-pass filter is employed. This is a significant result, because unlike the previously reported cases for transparent conductive oxide photocatalysts, such as N-doped TiO_2 nanotubes coated with a thin TaO_xN_y layer,[40] H_2-treated TiO_2 nanowires,[21] Fe_2TiO_5 coated TiO_2 nanotube arrays,[41] and very dense Si-core TiO_2-shell nanowire arrays,[38] where the observed photocurrent densities in AM 1.5G light were found to reduce by over 80% with visible light illumination, the observed reduction by only 31% makes the partially delaminated hierarchical nanowires the best photocatalyst for photoelectrochemical water splitting driven by the visible light.

In order to further verify that the observed photocurrent originates from the photoelectrochemical water splitting reaction rather than any other undesirable side reactions, in situ quantification of the evolved gases is performed by using a Stanford Research Systems Universal Gas Analyzer system. As shown in Figure S7 (Supporting Information), only the partial pressures of H_2 and O_2 are found to increase as the reaction commences, while those of the background gases (N_2, H_2O, and CO_2) remain flat and unchanged. The pressure change for H_2 ($\Delta P = 5.0 \times 10^{-5}$ Torr) is found to be almost twice that of O_2 ($\Delta P = 2.4 \times 10^{-5}$ Torr) upon reaching steady state after 120 min of reaction, which confirms the stoichiometric splitting of water. The corresponding Faradaic efficiency is estimated to be 97.8% (with detailed calculation given in the Supporting Information), which indicates that the photocurrent indeed comes from the water splitting reaction. More importantly, the amount of steady-state H_2 evolution (i.e., after 120 min of reaction) for hierarchical ZrO_2 nanowire film (638.60 μmol cm^{-2}) is found to be 270.6, 5.6, and 1.9 times those of HF-treated Si (2.36 μmol cm^{-2}), ZrO_2 nanobrick film (113.67 μmol cm^{-2}), and ZrO_2 nanowire film (332.07 μmol cm^{-2}), respectively (Figure 6d). The observed H_2 evolution amounts are in accord with the trend of photocurrent density (Figure 6b). These results therefore suggest that there are no reactions other than the photoelectrochemical water splitting reaction in the present case. More importantly, our photocatalysts are robust and their high photocurrent density remains unchanged even after 24 h of continuous photoelectrochemical water splitting reaction (Figure S8, Supporting Information). Similar stability tests have also been made for other nanostructured films and they also show virtually no degradation over repeated cycling and extended use. For HF-treated hierarchical nanowire film photocathode, the half-cell solar-to-hydrogen conversion efficiency is estimated to be 3.1% from the expression,[42] $[|J| \times \eta_F \times (V_{th} - V)]/P_{in} \times 100\%$, where J is the photocurrent density (mA cm^{-2}) under AM 1.5G illumination, η_F is the Faradaic efficiency, V_{th} is the theoretical voltage for H_2 generation in an acidic medium (0 V vs RHE), V is the absolute value of the applied potential (vs RHE), and P_{in} is the irradiance of the AM 1.5 G light (100 mW cm^{-2}).

We also investigate the wavelength-dependent incident photon-to-current conversion efficiency (IPCE) by coupling the AM 1.5 G filter separately with the 400, 500, 600, 700, and 800 nm bandpass filters (each with a full width at half maximum of 10 nm). For all the HF-treated films, the observed photoconversion efficiencies are the highest in the 500–600 nm region, and they closely correlate with the relative light intensity wavelength profile of natural sunlight (**Figure 7**a), with the maximum at 500 nm. For instance, the IPCE of the hierarchical nanowire film reaches 60–80% in the 500–600 nm region and then falls off in the longer wavelength region. The HF-treated regular nanowire film also shows similar IPCE profile shape but with the efficiency generally 20–40% lower than the HF-treated hierarchical nanowire sample. For the HF-treated nanobrick film, a relatively "flat" photoconversion profile with a maximum at 600 nm and a significantly lower efficiency (50–70%) than the HF-treated hierarchical nanowire sample is obtained. The observed photoresponses as indicated by the IPCE profiles are also consistent with the respective bandgaps derived from the corresponding Tauc plots (Figure 7b), which are determined to be 2.5, 2.8, 3.2, and 3.9 eV for HF-treated ZrO_2 hierarchical nanowire, regular nanowire, nanobrick, and commercial ZrO_2 powder samples, respectively. The relatively higher photocurrent response of the hierarchical nanowire sample at longer wavelength therefore suggests that they have more defect states in the band structure than the regular nanowire sample, resulting in a higher collection of photogenerated charge carriers. The lower photoresponse found for the regular nanowire and nanobrick films can also be attributed to their larger thicknesses and smaller surface areas. On the other hand, the markedly different photoresponse observed for the nanobrick film suggests that the nanobricks might have different defect compositions, with different defect state distributions in the band structure, when compared to the regular nanowires and hierarchical nanowires.

The lower photoelectrochemical activity of the as-grown nanostructured films than the corresponding partially delaminated nanostructured films could be attributed to a thicker SiO_2 buffer layer between the film and the Si substrate, and the lack of an amorphous ZrO_2 layer on the surface of crystalline ZrO_2. The thicker SiO_2 layer impedes the direct transfer of photogenerated carriers from the ZrO_2 film to the Si substrate (and onto the Pt counter electrode). On the other hand, the increased contact of the electrolyte due to buckling could also increase the possibility of back electron transfer from the solution to the current collector.[43] This effect is evidently well compensated by the numerous advantages of the thin amorphous layer in the buckled films. First, the amorphous layer on the underside surface of the buckled film improves the direct contact between the base of the nanostructured film and the Si substrate, which in turn reduces the diffusion length of the photogenerated carriers and consequently the recombination losses, in contrast to the as-grown film where the photogenerated carriers have to travel across the entire film to reach the external contact. Second, the amorphous layer with large numbers of undercoordinated metal atoms and of nonstoichiometric oxygen vacancy defects not only provides a great number of photoelectrochemical active sites that are not limited by their crystal structures, but also provides electron/hole traps that could lead to charge recombination.[44] The significantly improved photoelectrochemical activity of delaminated films suggests that the small thickness (3–5 nm) of the amorphous layer and

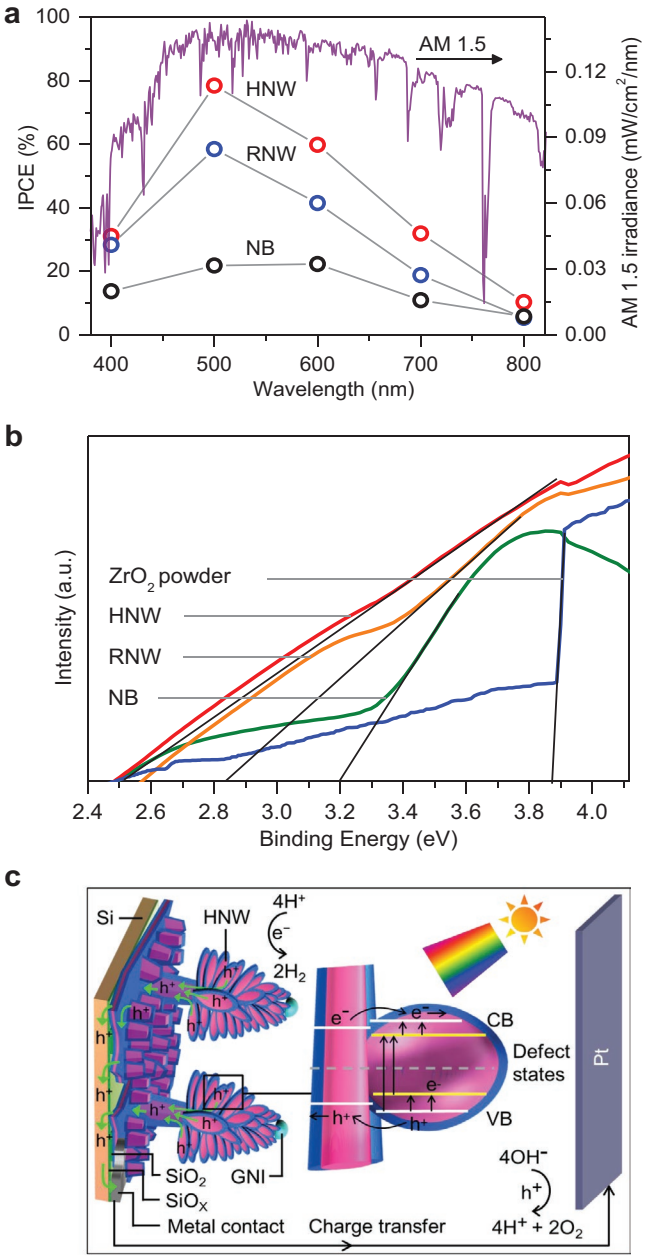

Figure 7. a) Incident photon-to-charge conversion efficiency profiles of HF-treated ZrO_2 hierarchical nanowire (HNW), regular nanowire (RNW), and nanobrick (NB) films as functions of wavelength at the applied voltage that gives the maximum HC-STH conversion efficiency [0.2 V (vs RHE)]. The irradiance spectrum is also shown for AM 1.5 solar radiation. b) Tauc plots for HF-treated ZrO_2 nanostructures and commercial ZrO_2 powders. c) Schematic diagram for the charge separation and transfer process in the nanoplates of the HF-treated ZrO_2 hierarchical nanowires in a photoelectrochemical water splitting reaction driven by visible light irradiation. Similar process involving their corresponding defect states [located between the valence band minimum (VB) and conduction band maximum (CB)] is expected to occur also in the amorphous shells and trunks of these nanowires.

the single-crystalline core backbone could significantly reduce recombination. This is because the photogenerated charge carriers can be readily separated and collected by the crystalline core backbone, as the diffusion length of photogenerated charge carriers is higher than the recombination length when compared to a completely amorphous electrode.[45] Finally, the buckling of the base nanostructured film after the HF treatment could potentially double the surface area and the amount of catalytically active sites. The buckling and the formation of an amorphous layer on the surface of crystalline oxides therefore significantly improve the photoelectrochemical performance of the as-grown ZrO_2 nanostructures.

For the HF-treated films, we also investigate the role of morphology and the amounts of defects on their photoelectrochemical performance to better understand their photoelectrochemical behavior. For the partially delaminated nanostructured films, the lower photocatalytic activity of the nanobrick film than the regular nanowire and hierarchical nanowire films is due to their smaller specific surface area available for the water reduction reaction. As shown in Table S3 (Supporting Information), the estimated specific surface area for a single ZrO_2 hierarchical nanowire (0.53 nm^{-1}) is found to be 1.7 and 17.7 times those of a regular nanowire (0.31 nm^{-1}) and a nanobrick (0.03 nm^{-1}), respectively. On the other hand, the higher photocatalytic activity of the hierarchical nanowire film compared to the regular nanowire film is attributed to the different morphologies of the nanowires. In the hierarchical nanowires, the densely packed nanoplates (10–20 nm thick) along individual nanowire trunks evidently provide significantly higher surface area for the photoelectrochemical reaction. In addition, the higher amount of oxygen vacancy defects in the hierarchical nanowires (Figure 5; and Table S1, Supporting Information) suggests the presence of more defect states in the bandgap, which ultimately enhance light absorption and generate more charge carriers for the water reduction reaction.

As reported for the other material systems,[46–48] both the bandgap and the deviation from stoichiometry (oxygen vacancy) increase with decreasing crystallite size. In the hierarchical nanowire, the thickness of the nanoplates (3–6 nm) is much smaller than the diameter of the trunk of the nanowire (30–40 nm). The nanoplates of hierarchical nanowire, therefore, have larger bandgap and higher content of oxygen vacancy defects. As the singly charged oxygen vacancy reduces Zr^{4+} ions to Zr^{3+} ions and generates one electron and one hole in the vacancy site, while the doubly charged oxygen vacancy leads to two Zr^{3+} ions or to one Zr^{2+} ion and two holes in the defect states, intermixing of the Zr^{4+}, Zr^{3+}, and Zr^{2+} ion states and their corresponding hole states at the defect sites could generate donor bands below the conduction band minimum and acceptor bands above the valence band maximum, respectively.[49,50] As a result, in the hierarchical nanowires, photogenerated carriers could migrate not only through the conduction band minimum but also through the mid-gap states, originating from these oxygen vacancy defects. The higher photoresponse of hierarchical nanowire film (Figure 7a) suggests that these mid-gap states improve light absorption and cause electrons to get trapped, screening them from charge recombination with holes and/or electrolyte,[51] consistent with the higher light absorption (Figure S5, Supporting Information) and photocurrent density (Figure 6b) found for the hierarchical nanowires. Efforts are underway to study the charge transfer dynamics and recombination processes in oxygen-vacancy rich ZrO_2 systems.

A schematic diagram for the enhancement mechanism of photoelectrochemical water splitting reaction of the partially delaminated hierarchical nanowire film is shown in Figure 7c. When the hierarchical nanowires are irradiated with AM 1.5G light, electron transfer takes place from both the valence band and oxygen vacancy defect states to the conduction band of ZrO_2. The photon-excited electrons in the nanoplates react with the acceptor species (H^+) of the electrolyte and generate H_2, while the photogenerated holes of the nanoplates injected into the valence band oxidize OH^- to produce O_2 at the Pt counter electrode. Owing to the single-crystalline nature of the core nanowire and to the direct contact between the nanostructured film and the Si substrate, the photogenerated holes in the valance band of the nanowire could migrate easily to the Si substrate and ultimately to the counter electrode. Similar process involving their corresponding defect states is also expected to occur in the trunks of these nanowires. The higher photocurrent density obtained from the partially delaminated hierarchical ZrO_2 nanowires can therefore be attributed to the dense mat of nanowires[52] with densely packed ZrO_2 nanoplates in individual nanowires. The presence of these nanoplates offers excellent light-trapping characteristics and a large contact area with the electrolyte, while their much smaller thickness and the presence of a large number of oxygen vacancy defect states not only facilitate the radial collection of minority carriers over a shorter distance but also improve the efficiency of the charge separation process and minimize the probability of recombination. Their combined effects give rise to superior photoelectrochemical performance in the visible region.

With a photocurrent density of –12.9 mA cm^{-2} (at 0 V vs RHE), the as-grown ZrO_2 hierarchical nanowire film is the best transparent conductive oxide nanostructured photocathode reported to date.[53] Even more phenomenal is the partially delaminated hierarchical nanowire film, which outperforms not only the best such transparent conductive oxide-based photocatalysts by a wide margin but indeed the best photocathode (including arrayed and more complex catalysts) reported to date (Table S4, Supporting Information). The measured photocurrent density for the partially delaminated hierarchical nanowire film (–42.5 mA cm^{-2} at 0 V vs RHE) is significantly higher than those modified p-type planar and 1D nanomaterials, including amorphous MoS_{2+x} coated TiO_2/n-AZO/p-Cu_2O composite films (–7.7 mA cm^{-2}),[54] Pt nanoparticle decorated planar p-Si (–23.3 mA cm^2)[55] and p-Si nanowire array (–20 mA cm^{-2}),[56] Pt implanted TiO_2/Cu(In,Ga)Se_2 composite photocathode device (–15 mA cm^{-2}),[57] Pt/TiO_2/Ti/n^+pp^+–Si heterostructure (–25 mA cm^{-2}),[19] and a Pt/TiO_2/Al_2O_3/ZnO protective layer coated Cu_2O thin film (–5.7 mA cm^{-2}).[9] Indeed, the photocurrent density of the partially delaminated hierarchical nanowire film is also higher than the best photocathodes reported to date, including $NiCoSe_x$/p–Si shell/core nanopillar array (–37.5 mA cm^{-2}),[58] CoPS/n^+pp^+–Si micropyramids (–35 mA cm^{-2}),[59] and a nitrogen-doped graphene quantum nanosheet decorated p–Si nanowire array (–35 mA cm^{-2}).[60] The record-high performance of the present photoelectrode (–42.5 mA cm^{-2} at 0 V vs RHE) is especially remarkable when considering the smaller length (1 μm) and lower density of the hierarchical nanowires than those reported in the literature.[56,58,60] In order to achieve the reported current density of –20 to –37.5 mA cm^{-2}, these latter nanowires were produced with considerably higher areal density and average length of 5–15 μm, in order to provide more active sites for the photoelectrochemical reaction. Furthermore, the present photocathode is found to be highly stable in harsh acidic conditions (Figure S8, Supporting Information) and the majority (>70%) of its photocurrent comes from the visible part of the AM 1.5 G spectrum (Figure 6c). The rate of hydrogen evolution (890 μmol cm^{-2} h^{-1}) is also found to be considerably higher than the reported photoelectrodes, including Al_2O_3/NiO (1.09 μmol cm^{-2} h^{-1}),[61] $CuNb_3O_8$ (3.5 μmol cm^{-2} h^{-1}),[62] and a Pt loaded In_2S_3/$CuInS_2$ p–n junction electrode (232.6 μmol cm^{-2} h^{-1}).[63] Even more remarkable is that the present half-cell solar-to-hydrogen efficiency (3.1%) is significantly higher than the reported photocathodes, including wafer-scale MoS_2/p–Si heterojunction electrode (0.68%),[64] hybrid Pt-TiO_2/P3HT:PCBM/CuI/FTO microstructure (1.21%),[65] Pt loaded In_2S_3/$CuInS_2$ p–n junction electrode (1.97%),[63] and a Pt–TiO_2/Cu(In,Ga)Se_2 composite photocathode device (2%).[57] In order to reach these efficiencies, these latter studies require the use of expensive cocatalysts and employ elaborate multistep synthesis procedures for the preparation of the photoelectrodes. This is in marked contrast to the present photocathode, which only requires an inexpensive material and a one-step catalyst-assisted pulsed laser deposition method. The simple HF post-treatment used in the present work that introduces buckling and formation of a thin amorphous layer on the single-crystalline nanostructured film can also be used to provide additional enhancement in the photoelectrochemical performance for other hierarchical nanostructured films of TiO_2 and Ta_2O_5 (not shown). This work therefore demonstrates that the simple post-treatment is a facile approach to improve the photoelectrochemical performance of crystalline metal-oxide nanostructure films, which promises rational design and effective preparation of other composite photoelectrodes for photoelectrochemical applications.

3. Conclusion

In summary, the use of a high vacuum system and precise control of the growth temperature and Ar flow have enabled us to produce, for the first time, defect-rich, single-crystalline nanostructured ZrO_2 films with different compositions of oxygen vacancy defects. We further demonstrate that post-treatment with dilute HF solution introduces buckling and a thin amorphous ZrO_2 shell into the nanostructured film, which dramatically reduce (by over three orders of magnitude) the charge transport resistance and also increase the active area exposed to the electrolyte and the amount of oxygen vacancy defects. Photoelectrochemical measurement under simulated sunlight at one sun shows that the partially delaminated hierarchical nanowires exhibit an extraordinary photocurrent density (–42.5 mA cm^{-2}, at 0 V vs RHE), more than tripling that of the as-grown hierarchical nanowires (–12.9 mA cm^{-2}). Even more remarkable is that 69% of its photoactivity comes from the visible part of the sunlight spectrum. With an estimated 3.1% half-cell solar-to-hydrogen conversion efficiency, the present partially delaminated hierarchical ZrO_2 nanowire

photocatalysts therefore offer a potentially viable commercial solution for solar hydrogen production.

The record high performance of the present photoelectrode could be further increased by increasing the areal density of the nanowires (e.g., by increasing the GNI areal density) and/or the length of the nanowires (e.g., by increasing the deposition time). An even higher efficiency can be achieved by adapting more elaborate strategies including fabricating hybrid and/or core–shell nanowires and synthesizing binary or tertiary nanowires, which can be easily accomplished by switching the targets (using a multitarget holder in our PLD system) during growth of the ZrO_2 nanowires. More importantly, the present approach of intentionally growing defect-rich nanowires both chemically (by introducing oxygen vacancy defects) and mechanically (by partial delamination and introduction of hierarchical architectures) by catalyst-assisted PLD growth followed by a simple HF treatment has created a new class of (defect-rich) materials. This approach could be extended to other wide bandgap semiconductors and their solar visible-light driven applications, including photoelectrochemical water splitting, photocatalysis, and solar cells.

Supporting Information

Supporting Information is available from the Wiley Online Library or from the author.

Acknowledgements

This work was supported by the Natural Sciences and Engineering Research Council of Canada. Md A.R. and K.T.L. conceptualized and designed the project. Md A.R. synthesized and characterized the ZrO_2 nanostructured thin films, fabricated the devices, and analyzed the results. J.P.T. obtained the TEM images. The manuscript was written by Md A.R. and K.T.L. All authors discussed the results and commented on the manuscript.

Conflict of Interest

The authors declare no conflict of interest.

Keywords

nanostructured photocathodes, oxygen vacancy defects, p-type zirconium dioxides, transparent conductive oxides, visible-light-driven photoelectrochemical water splitting

Received: May 5, 2017
Revised: July 1, 2017
Published online: September 22, 2017

[1] A. A. Agrawal, A. P. Hastings, M. T. J. Johnson, J. L. Maron, J. Salminen, *Science* **2010**, *329*, 1330.
[2] M. I. Hoffert, *Science* **2010**, *329*, 1292.
[3] J. Hill, E. Nelson, D. Tilman, S. Polasky, D. Tiffany, *Proc. Natl. Acad. Sci. USA* **2006**, *103*, 11206.
[4] N. S. Lewis, *Science* **2007**, *315*, 798.
[5] D. C. Bookbinder, J. A. Bruce, R. N. Dominey, N. S. Lewis, M. S. Wrighton, *Proc. Natl. Acad. Sci. USA* **1980**, *77*, 6280.
[6] A. Kay, I. Cesar, M. Grätzel, *J. Am. Chem. Soc.* **2006**, *128*, 15714.
[7] S. U. M. Khan, M. Al-Shahry, W. B. Ingler, *Science* **2002**, *297*, 2243.
[8] V. R. Reddy, D. W. Hwang, J. S. Lee, *Korean J. Chem. Eng.* **2012**, *20*, 1026.
[9] A. Paracchino, V. Laporte, K. Sivula, M. Grätzel, E. Thimsen, *Nat. Mater.* **2011**, *10*, 456.
[10] O. Khaselev, J. A. Turner, *Science* **2013**, *280*, 425.
[11] E. Aharon-Shalom, A. Heller, *J. Electrochem. Soc.* **1982**, *129*, 2865.
[12] J. Tang, J. R. Durrant, D. R. Klug, *J. Am. Chem. Soc.* **2008**, *130*, 13885.
[13] A. L. Linsebigler, J. T. Yates Jr., G. Lu, G. Lu, J. T. Yates, *Chem. Rev.* **1995**, *95*, 735.
[14] X. Chen, C. Burda, *J. Am. Chem. Soc.* **2008**, *130*, 5018.
[15] W. Choi, A. Termin, M. R. Hoffmann, *J. Phys. Chem.* **1994**, *98*, 13669.
[16] J. Du, J. Qi, D. Wang, Z. Tang, *Energy Environ. Sci.* **2012**, *5*, 6914.
[17] H. Yin, S. Zhao, K. Zhao, A. Muqsit, H. Tang, L. Chang, H. Zhao, Y. Gao, Z. Tang, *Nat. Commun.* **2015**, *6*, 6430.
[18] X. Ma, K. Zhao, H. Tang, Y. Chen, C. Lu, W. Liu, Y. Gao, H. Zhao, Z. Tang, *Small* **2014**, *10*, 4664.
[19] D. Bae, T. Pedersen, B. Seger, M. Malizia, A. Kuznetsov, O. Hansen, I. Chorkendorff, P. C. K. Vesborg, *Energy Environ. Sci.* **2015**, *8*, 650.
[20] J. Hou, C. Yang, H. Cheng, S. Jiao, O. Takeda, H. Zhu, *Energy Environ. Sci.* **2014**, *7*, 3758.
[21] G. Wang, H. Wang, Y. Ling, Y. Tang, X. Yang, R. C. Fitzmorris, C. Wang, J. Z. Zhang, Y. Li, *Nano Lett.* **2011**, *11*, 3026.
[22] J. Nai, H. Yin, T. You, L. Zheng, J. Zhang, P. Wang, Z. Jin, Y. Tian, J. Liu, Z. Tang, L. Guo, *Adv. Energy Mater.* **2015**, *5*, 1401880.
[23] J. Y. Kim, G. Magesh, D. H. Youn, J. Jang, J. Kubota, K. Domen, J. S. Lee, *Sci. Rep.* **2013**, *3*, 2681.
[24] J. Y. Lee, J. Park, J. H. Cho, *Appl. Phys. Lett.* **2005**, *87*, 2014.
[25] H. Yeon, S. Lim, J. Jung, H. Yoo, Y. Lee, H. Kang, Y. Park, M. Kim, Y. Joo, *NPG Asia Mater.* **2016**, *8*, e250.
[26] J. Highfield, *Molecules* **2015**, *20*, 6739.
[27] G. S. Zhdanov, *Crystal Physics*, Academic Press, New York **1965**.
[28] K. Zhu, N. R. Neale, A. Miedaner, A. J. Frank, *Nano Lett.* **2007**, *7*, 69.
[29] M. A. Rahman, S. Bazargan, S. Srivastava, X. Wang, M. Abd-Ellah, J. P. Thomas, N. F. Heinig, D. Pradhan, K. T. Leung, *Energy Environ. Sci.* **2015**, *8*, 3363.
[30] T. Bauer, Thermophotovoltaics: Basic Principles and Critical Aspects of System Design, Springer, Berlin **2011**.
[31] T. B. Massalski, H. Okamoto, J. P. Abriata, *Bull. Alloy Phase Diagrams* **1985**, *6*, 519.
[32] J. Shi, X. Wang, *Cryst. Growth Des.* **2011**, *11*, 949.
[33] J. F. Chang, T. F. Young, Y. L. Yang, H. Y. Ueng, T. C. Chang, *Mater. Chem. Phys.* **2004**, *83*, 199.
[34] R. D. L. Smith, *Science* **2013**, *340*, 60.
[35] M. V. Ganduglia-Pirovano, A. Hofmann, J. Sauer, *Surf. Sci. Rep.* **2007**, *62*, 219.
[36] E. Hildebrandt, J. Kurian, M. M. Muller, T. Schroeder, H. J. Kleebe, L. Alff, *Appl. Phys. Lett.* **2011**, *99*, 112902.
[37] A. Tsukazaki, A. Ohtomo, T. Onuma, M. Ohtani, T. Makino, M. Sumiya, K. Ohtani, S. F. Chichibu, S. Fuke, Y. Segawa, H. Ohno, H. Koinuma, M. Kawasaki, *Nat. Mater.* **2004**, *4*, 42.
[38] Y. J. Hwang, A. Boukai, P. Yang, *Nano Lett.* **2009**, *9*, 410.
[39] H. Jiang, R. I. Gomez-Abal, P. Rinke, M. Scheffler, *Phys. Rev. B* **2010**, *81*, 1.
[40] H. Kim, D. Monllor-Satoca, W. Kim, W. Choi, *Energy Environ. Sci.* **2015**, *8*, 247.
[41] Q. Liu, J. He, T. Yao, Z. Sun, W. Cheng, S. He, Y. Xie, Y. Peng, H. Cheng, Y. Sun, Y. Jiang, F. Hu, Z. Xie, W. Yan, Z. Pan, Z. Wu, S. Wei, *Nat. Commun.* **2014**, *5*, 5122.
[42] T. Hisatomi, J. Kubota, K. Domen, *Chem. Soc. Rev.* **2014**, *43*, 7520.
[43] M. J. Kang, Y. S. Kang, *J. Mater. Chem. A* **2015**, *3*, 15723.
[44] J. Liu, S. Wen, Y. Hou, F. Zuo, G. J. O. Beran, P. Feng, *Angew. Chem., Int. Ed.* **2013**, *52*, 3241.

[45] Y. P. Dan, K. Seo, K. Takei, J. H. Meza, A Javey, K. B. Crozier, *Nano Lett.* **2011**, *11*, 2527.
[46] L. Kong, C. Wang, H. Zheng, X. Zhang, Y. Liu, *J. Phys. Chem. C* **2015**, *119*, 16623.
[47] W. Li, A. Kuc, C. F. J. Walther, T. Heine, *J. Phys. Chem. A* **2015**, *119*, 5742.
[48] A. Teleki, S. E. Pratsinis, *Phys. Chem. Chem. Phys.* **2009**, *11*, 3742.
[49] G. Li, Z. Lian, X. Li, Y. Xu, W. Wang, D. Zhang, F. Tian, H. Li, *J. Mater. Chem. A* **2015**, *3*, 3748.
[50] F. M. Hossain, G. E. Murch, *Defect Diffus. Forum* **2006**, *251–252*, 1.
[51] J. Ran, T. Y. Ma, G. Gao, X.-W. Du, S. Z. Qiao, *Energy Environ. Sci.* **2015**, *8*, 3708.
[52] S. Bazargan, K. T. Leung, *J. Chem. Phys.* **2013**, *138*, 104704.
[53] N. K. Awad, E. A. Ashour, N. K. Allam, *J. Renewable Sustainable Energy* **2014**, *6*, 022702.
[54] C. G. Morales-Guio, S. D. Tilley, H. Vrubel, M. Grätzel, X. Hu, *Nat. Commun.* **2014**, *5*, 3059.
[55] J. R. McKone, E. L. Warren, M. J. Bierman, S. W. Boettcher, B. S. Brunschwig, N. S. Lewis, H. B. Gray, *Energy Environ. Sci.* **2011**, *4*, 3573.
[56] N. P. Dasgupta, C. Liu, S. Andrews, F. B. Prinz, P. Yang, *J. Am. Chem. Soc.* **2013**, *135*, 12932.
[57] A. Azarpira, M. Lublow, A. Steigert, P. Bogdanoff, D. Greiner, C. A. Kaufmann, M. Krüger, U. Gernert, R. Van De Krol, A. Fischer, T. Schedel-Niedrig, *Adv. Energy Mater.* **2015**, *5*, 1402148.
[58] H. Zhang, Q. Ding, D. He, H. Liu, W. Liu, Z. Li, B. Yang, X. Zhang, L. Lei, S. Jin, *Energy Environ. Sci.* **2016**, *9*, 3113.
[59] M. Cabán-Acevedo, M. L. Stone, J. R. Schmidt, J. G. Thomas, Q. Ding, H. Chang, M. Tsai, J. He, S. Jin, *Nat. Mater.* **2015**, *14*, 1245.
[60] U. Sim, J. Moon, J. An, J. H. Kang, S. E. Jerng, J. Moon, S. Cho, B. H. Hong, K. T. Nam, *Energy Environ. Sci.* **2015**, *8*, 1329.
[61] C. Hu, K. Chu, Y. Zhao, W. Y. Teoh, *ACS Appl. Mater. Interfaces* **2014**, *6*, 18558.
[62] U. A. Joshi, P. A. Maggard, *J. Phys. Chem. Lett.* **2012**, *3*, 1577.
[63] Gunawan, W. Septina, S. Ikeda, T. Harada, T. Minegishi, K. Domen, M. Matsumura, *Chem. Commun.* **2014**, *50*, 8941.
[64] K. C. Kwon, S. Choi, K. Hong, C. W. Moon, Y. Shim, D. H. Kim, T. Kim, W. Sohn, J. Jeon, C. Lee, K. T. Nam, S. Han, S. Y. Kim, H. W. Jang, *Energy Environ. Sci.* **2016**, *9*, 2240.
[65] H. Rojas, S. Bellani, F. Fumagalli, G. Tullii, S. Leonardi, M. T. Mayer, M. Schreier, M. Grätzel, G. Lanzani, F. Di Fonzo, M. R. Antognazza, *Energy Environ. Sci.* **2016**, *9*, 3710.